Volume 13
Number 11
21 March 2025
Pages 7585–8204

Journal of Materials Chemistry A

Materials for energy and sustainability

rsc.li/materials-a

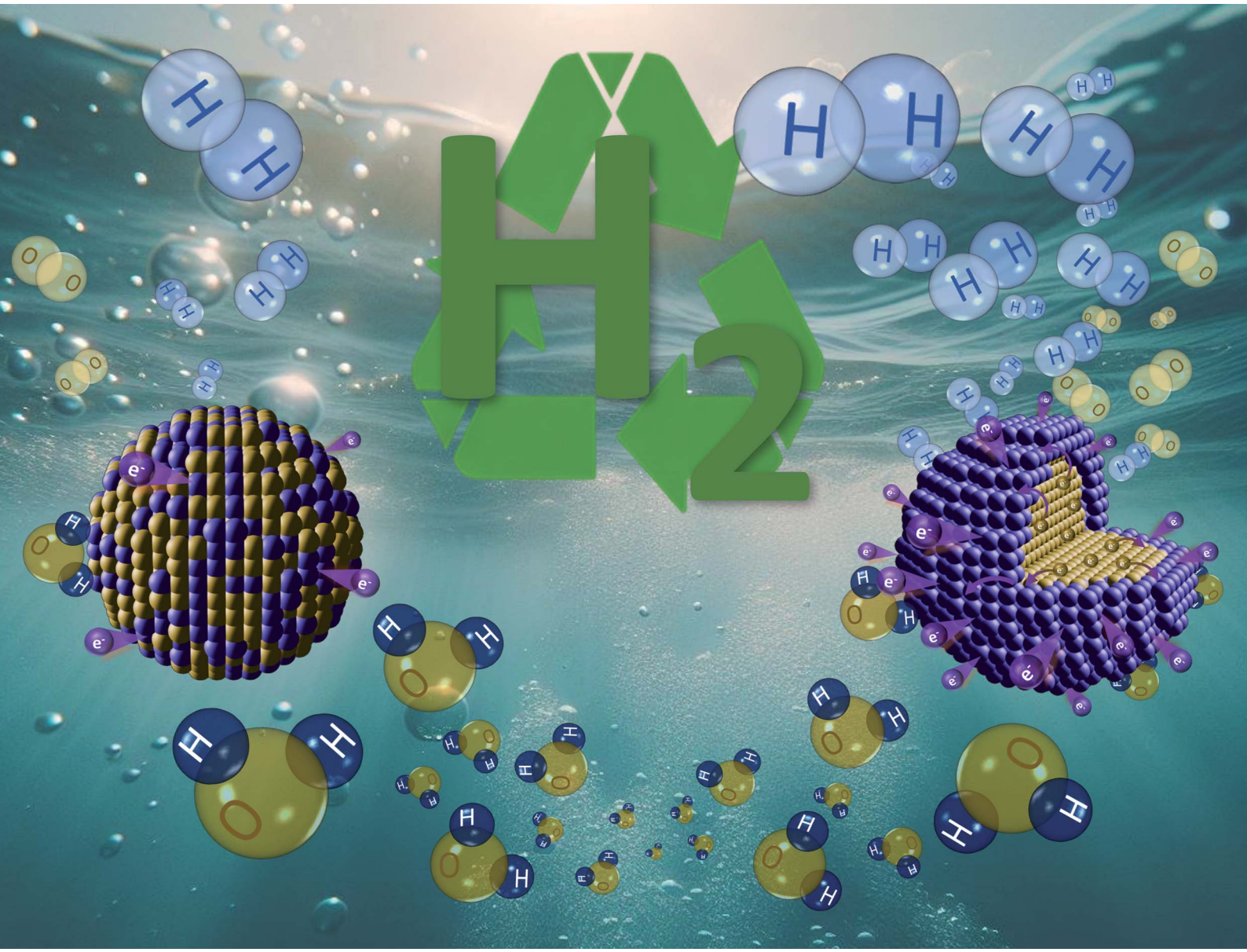

ISSN 2050-7488

ROYAL SOCIETY OF CHEMISTRY

PAPER

Pablo Guardia *et al.*

AuPt nanostructures with a high hydrogen evolution reaction activity through a halide-mediated microwave assisted route

Journal of Materials Chemistry A

ROYAL SOCIETY OF CHEMISTRY

PAPER

View Article Online
View Journal | View Issue

Cite this: J. Mater. Chem. A, 2025, 13, 7721

AuPt nanostructures with a high hydrogen evolution reaction activity through a halide-mediated microwave assisted route†

Xuesong Zhang,[a] Jesús Chacón-Borrero,[b] Ren He,[b] Jaume Gázquez,[a] Miquel Torras,[a] Andreu Cabot,[bc] Anna Roig[a] and Pablo Guardia *[a]

Received 1st July 2024
Accepted 8th October 2024

DOI: 10.1039/d4ta04545a

rsc.li/materials-a

In light of the escalating scarcity and rising costs of platinum, it is imperative to take a strategic approach to its rational utilization as an electrocatalyst for the hydrogen evolution reaction (HER). In this study, we present a novel microwave (MW)-assisted synthesis route combined with the addition of halide ions, specifically chloride, for the synthesis of AuPt nanostructured electrocatalysts. By adjusting the Au : Pt ratio in solution, as well as the halide concentration, we achieve control over the composition, size, shape, and structure of the nanocrystals (NCs). Comparative analysis of the HER electrocatalytic activity revealed that samples produced in the presence of chloride exhibit reduced overpotentials and increased mass activities. Notably, when using a 1 : 4 Au : Pt ratio and 0.12 mmol of HCl, NCs display lower overpotential and Tafel slope values compared to commercial platinum carbon (Pt/C) catalyst (24 mV @ 10 mA cm^{-2} and 13 mV dec^{-1} compared to 31 mV @ 10 mA cm^{-2} and 30 mV dec^{-1} respectively). Moreover, this nanostructure exhibits a 6.9 fold higher mass activity compared to Pt/C (13.8 A mg_{Pt}^{-1} and 2.0 A mg_{Pt}^{-1}, respectively). We attribute the enhancement in electrocatalytic performance to the formation of an Au-rich core supporting a Pt shell structure, which maximizes the exposure of Pt atoms. This synthesis route offers a pathway to produce Pt-based catalysts with superior electrocatalytic performance for HER, contributing to the rational use of Pt in green hydrogen production.

1 Introduction

Compared to synthetic carbon-based fuels, hydrogen holds the potential for achieving carbon neutrality or even a negative carbon footprint throughout its life cycle.[1] Nevertheless, more than 90% of the world's hydrogen is produced from fossil fuels, predominantly *via* steam methane reforming, with only 4% generated through water electrolysis.[2,3] Splitting water employing electrical current from renewable energy sources represents a zero CO_2 emission hydrogen production, commonly referred to as green hydrogen.[4] The water-splitting process encompasses two half-reactions, the hydrogen evolution reaction (HER) at the cathode and the oxygen evolution reaction (OER) at the anode. To overcome the energy barrier of these electrochemical processes, voltages as high as 1.8 V may be required. In this scenario, electrocatalysts are key actors in lowering high overpotentials (η), enhancing efficiency, and reducing the total energy consumption of hydrogen production.[5] Consequently, the development of active, stable, and cost-effective electrocatalysts for water-splitting is critical for a green hydrogen-based economy.

Non-noble metal catalysts, such as metal-sulfides, -nitrides and -phosphides nanomaterials, have attracted significant attention in the past decade.[6–8] Nevertheless, they exhibit lower stability and activity in water splitting compared to noble-metal catalysts (*e.g.* Pt, Ir or Ru).[9–11] Indeed, Pt-based catalysts deliver high current densities at low overpotentials for HER.[12–14] In that regard, despite their scarcity, the trade-off between the reduced energy consumption and the cost of Pt-based catalysts is considered advantageous. As such, the energy savings from lowering the cell operating voltage by 0.1 V can be up to ten times the cost of the Pt electrocatalyst.[15]

Multi-metallic nanocrystals (NCs) represent an appealing platform for developing low-Pt content catalysts providing unique physicochemical and catalytic properties resulting from the modulation of electronic states.[16–20] For instance, bimetallic (PtRu, Pt_3Ni, PtNi, Pt_3Co or Pt_3Fe)[21–23] or high entropy alloys (*e.g.*, FeCoNiPtIr)[24,25] have shown remarkable catalytic activity for low Pt loadings. In parallel, alternative strategies such as depositing a Pt atomic layer shell onto metallic cores,[26] single Pt atom decoration on carbon or metal oxides matrices,[27,28] or the

[a]Institut de Ciència de Materials de Barcelona (ICMAB-CSIC), Campus UAB, Bellaterra, 08193, Spain. E-mail: pguardia@icmab.es
[b]Catalonia Institute for Energy Research (IREC), Sant Adrià de Besòs, Barcelona, 08930, Spain
[c]ICREA, Pg. Lluis Companys, Catalonia, Barcelona, 08010, Spain

† Electronic supplementary information (ESI) available. See DOI: https://doi.org/10.1039/d4ta04545a

atomic Pt functionalization of porous structures[29,30] have reported noteworthy progresses in this field.

Among multi-metallic structures, Au-based alloys have garnered much attention in the last decade with a plethora of well-stablished synthetic approaches.[31,32] Despite the low binding energy and high overpotential of Au atoms for the HER,[33] alloyed electrocatalysts such as AuCu, AuPd, or AuNi have attracted interest due to their excellent activity combined with durability and low precious metal content.[34] In the particular case of AuPt alloys the combination of a Pt d-band shift with the proportional competencies of Au and Pt atoms has led to enhanced catalytic efficiency.[35] Moreover, Au stabilizes the Pt increasing the durability of AuPt catalysts by up to 30 times.[36]

The combination of Au and Pt into a structure has been proven to provide significant advances in the activity and stability of electrocatalysts for acidic HER. On the one hand, controlling the stoichiometry in AuPt bimetallic alloys has an impact in reducing overpotentials as reported for Au_1Pt_8 NCs with $\eta = 26$ mV at 10 mA cm^{-2}.[37] On the other hand, Au–Pt heterostructures such as $Au_{38.4}@Au_{9.3}Pt_{52.3}$ or Au@PtIr core–shell NCs have demonstrated also outstanding activites.[38,39] In that direction, strain engineering in $Au@PtCo_{0.05}$ core–shell structures has been reported to modulate the Pt d-band position.[40] Nowadays Au–Pt nanostructures are predominantly produced following two-step approaches (*e.g.* seed-mediated growth) thus increasing production costs while limiting mass production.[32] Simultaneously, ultra-small AuPt NCs (below 3 nm) or the control over shape are highly desirable despite its compromised stability.[41] Microwave (MW) assisted approaches have been successfully employed to produce metal or alloyed NCs but with limited control over the formation of complex structures such as dumbbell like or core–shell alloys.[42,43] In that regard, halide ions have been identified as shape directors in the synthesis of metallic NCs,[44–46] or as interphase mediators in the growth of semiconductor core–shell structures.[47–49] Noteworthy, the effect of halide ions in the synthesis of alloys has received limited attention, particularly within the context of MW-assisted synthesis approaches.

Herein, we report on the MW-assisted synthesis of AuPt bimetallic NCs showing exceptional performance as electrocatalysts for the HER under acidic conditions. These NCs were produced by exposing a solution containing Au and Pt precursors to a MW radiation for 10 min. By adjusting the Au to Pt precursor molar ratio, various shapes, including spheres, clusters, and peanut-shaped NCs were synthesized. Interestingly, the controlled addition of halide ions in the reaction solution, such as chloride, provided further control over the shapes resulting in the formation of core–shell structures. The electrocatalytic activity for the HER in acidic media revealed a significant correlation between the Au to Pt feeding ratio or the presence of chloride. Noteworthy, despite the inherent lack of activity for HER of Au, the AuPt core–shell structures showed remarkable activities, surpassing those of commercial Pt/C. In particular, overpotentials as low as 24 mV @ 10 mA cm^{-2} along with a mass activity up to 6.9 fold higher compared to that of commercial Pt/C. On the one hand, these results emphasize the primary influence of chloride in modulating the reaction kinetics of Au and Pt, leading to the growth of an Au-rich core surrounded by a thin Pt shell. On the other hand, the presence of an Au core appears to be responsible for the enhanced catalytic activity of AuPt NCs compared to state-of-the-art Pt and Pt-based catalysts. To the best of our knowledge, this is the first work investigating the effect of chloride ions and Au : Pt feeding ratios as size and shape modulators in the MW-assisted synthesis of AuPt NCs, as well as their effect on the electrocatalytic activity.

2 Experimental

2.1 Materials

Tetrachloroauric(III) acid trihydrate ($HAuCl_4 \cdot 3H_2O$, ≥99.9%), chloroplatinic acid hydrate ($H_2PtCl_6 \cdot xH_2O$, ≥99.9%), hydrochloric acid (HCl, 37%), polyvinylpyrrolidone (PVP_{10k}, $M_W = 10\,000$), sodium borohydride ($NaBH_4$, 99%), Nafion 117 (~5% solution in a mixture of lower aliphatic alcohols and water) and 2-propanol (≥99.5%) were purchased from Sigma-Aldrich. Ethylene glycol (EG, ≥99%), ethanol and acetone were purchased from Panreac. Carbon black (Vulcan CX-72) was purchased from FuelCellStore. Commercial Pt/C (20 wt% on Vulcan) was purchased from Quintech. Sulfuric acid (H_2SO_4, 98%) was purchased from Fisher Chemical. All materials were used as received without further purification. Milli-Q water (18.2 MΩ cm, Milli-Q IQ, Merck Millipore) was employed for all experiments and solutions.

2.2 Synthesis of AuPt NCs

Samples were synthesized in a MW reactor (CEM Discover SP) operating at a frequency of 2.45 GHz and a power of 300 W. Solutions were placed inside the reactor and heated to the desired temperature by applying MW radiation. Temperature control was achieved by applying pulsed MW radiation. The samples produced by the MW-assisted approach were compared to those synthesized using a conventional oil-bath approach.

MW-assisted synthesis of AuPt nanocrystals. In a standard procedure for the synthesis of AuPt NCs, 25 mg of PVP_{10k} was placed in a 10 mL reaction tube and dissolved in 4 mL of ethylene glycol by continuous sonication (*ca.* 20 min). Next, 5.6 μL and 22.4 μL of 289 mM solutions of $HAuCl_4 \cdot 3H_2O$ and $H_2PtCl_6 \cdot xH_2O$, respectively, were added to the reaction tube resulting in a homogeneous yellowish-colored solution. The final metal ion concentration was 2 mM (Au and Pt). The tube was placed in the MW reactor and heated up to 160 °C (*ca.* 90 seconds). After 10 min at this temperature, the reaction tube was cooled down and 30 mL of acetone was added, followed by centrifugation at 6000 rpm for 10 min. The supernatant was discarded, and the solid precipitate dispersed in 1 mL of MQ-H_2O. The NCs were further washed by adding 10 mL of acetone to the solution and centrifuging it at 6000 rpm for 10 min. This washing procedure was repeated at least twice before dispersing the final sample into 1 mL of MQ-H_2O. According to the Au to Pt molar feeding ratio, the sample was labelled as $AuPt_{1/4}$.

Samples with different Au : Pt molar ratios were synthesized by following the above-described procedure but varying the volumes of the Au and Pt metal stock solutions added to the reaction solution. Regardless of the Au : Pt ratio, the total volume of the metal solutions (Au and Pt) was kept constant (28 μL) resulting in a 2 mM final metal ion concentration. Samples were labelled according to the Au : Pt feeding molar ratio: Pt(0 : 1), $AuPt_{1/6}$(1 : 6), $AuPt_{1/4}$(1 : 4), $AuPt_{1/2}$(1 : 2), $AuPt_{1/1}$(1 : 1), $AuPt_{2/1}$(2 : 1), $AuPt_{4/1}$(4 : 1), $AuPt_{6/1}$(6 : 1), and Au(1 : 0).

Halide-mediated synthesis of AuPt NCs. Following the above-described procedure, a given amount of chloride was introduced into the solution by adding a hydrochloric acid solution (HCl, 37 wt%). For instance, 10 μL (122 μmol of HCl) were added into a 4 mL of ethylene glycol solution containing 25 mg of PVP_{10k}, 5.6 μL of $HAuCl_3 \cdot 3H_2O$ solution (289 mM) and 22.4 μL of $H_2PtCl_6 \cdot xH_2O$ solution (289 mM). The remaining procedures were identical to the ones described above, and these samples were labelled as $AuPt_{1/4Cl}$. Various samples (Pt_{Cl}, $AuPt_{1/6Cl}$, $AuPt_{1/4Cl}$, $AuPt_{1/2Cl}$, $AuPt_{1/1Cl}$, $AuPt_{2/1Cl}$, $AuPt_{4/1Cl}$, $AuPt_{6/1Cl}$, Au_{Cl}) were produced by varying the Au : Pt ratios while keeping the HCl amount constant (0 : 1, 1 : 6, 1 : 4, 1 : 2, 1 : 1, 2 : 1, 4 : 1, 6 : 1, and 1 : 0, respectively).

Ligand removal. The above-produced NCs were coated by PVP molecules, forming an organic shell that may potentially interfere with the activity of the electrocatalysts. Therefore, PVP was removed from the surface of the AuPt NCs following a reported approach with minor modifications.[50] In a typical procedure, 10 mg of $AuPt_{1/4Cl}$ NCs were dispersed by sonication in 20 mL of a $NaBH_4$/ethanol/H_2O solution (10 mg/10 mL/10 mL) for 3 min at room temperature. After sonication, 30 mL of ethanol were added to the mixture and NCs were collected by centrifugation (10 000 rpm, 20 min). The precipitate was then washed three times with ethanol and collected by centrifugation (10 000 rpm, 20 min) before being dried under ambient conditions and stored as a powder.

2.3 NCs characterization

The detail of characterizations of NCs are provided in ESI.†

2.4 Electrochemical characterization

Catalyst preparation. The NCs produced were supported on carbon black to assess their electrocatalytic activity. Specifically, 4 mg of AuPt NCs and 32 mg of carbon black (1 : 8 weight ratio) were mixed in ethanol through continuous sonication for 3 h to ensure a uniform dispersion of AuPt NCs on carbon black. After drying the suspension under vacuum at 60 °C for 6 h, 4 mg of the catalysts (AuPt NCs and carbon black) were mixed with 1 mL of a solution containing 220 μL of MQ-H_2O, 750 μL of 2-propanol and 30 μL of Nafion. The mixture was then sonicated for 30 min until a homogeneous ink was formed.

Electrocatalytic performance. All electrochemical measurements were conducted at room temperature using a CHI760E electrochemical workstation (Shanghai Chenhua Instrument Co. Ltd., China). A standard three-electrode cell configuration with a glassy carbon (5 mm in diameter) and graphite electrodes as the working (WE) and counter (CE) electrodes, and an Ag/AgCl electrode as the reference (RE) was used. The WE was prepared by polishing the surface before drop casting 5 μL of the AuPt NCs ink (see section above). The final Au and Pt metal loadings were determined by ICP-OES for each sample (see Table 1). Linear sweep voltammetry (LSV) was conducted at a scan rate of 5 mV s^{-1} from 0 to −0.6 V (*vs.* Ag/AgCl) in a 0.5 M H_2SO_4 electrolyte. All potentials were corrected to the reversible hydrogen electrode (RHE) by following the Nernst equation: $E_{RHE} = E_{Ag/AgCl} + 0.0591pH + 0.197$ V. All the data were corrected for the 90% *iR* compensation within the cell. The electrochemical double-layer capacitance (C_{dl}) curves of the catalysts were measured by cyclic voltammetry (CV) in the non-faradaic region (0.397–0.497 V *vs.* RHE) at scan rates from 20 to 200 mV s^{-1}. The C_{dl} was calculated by following the equation: $C_{dl} = \Delta j/\nu$, where Δj ($\Delta j = (j_a - j_c)/2$) and ν are the current density (at 0.447 V, mA cm^{-2}) and scan rate (mV s^{-1}), respectively. From the C_{dl}, the electrochemical active surface area (ECSA) was calculated as: ECSA = C_{dl}/C_s, where the general specific capacitance (C_s) was 0.035 mF cm^{-2} in 0.5 M H_2SO_4. Electrochemical impedance spectra (EIS) were acquired with an amplitude of 5 mV at frequencies ranging from 10^6 to 0.01 Hz. The stability of catalysts was tested by running for 4000 cycles (accelerated scan rate 200 mV s^{-1}) at a potential amplitude between −0.05 and −0.15 V *vs.* RHE. Stability over time was evaluated by voltage–time plots keeping a constant current density of 10 mA cm^{-2}. Finally, the mass activity of the catalyst was calculated according to the following equations: $m_{activity} = j/m_{pt}$ or j/m_{Au+pt}, where j is the measured current density (mA cm^{-2}) and m is the loading of Pt or Au + Pt inside the catalyst (*i.e.*, Pt/(Au + Pt) mg cm^{-2}).

3 Results and discussion

According to the literature, halide atoms have been explored in the synthesis of Au and Ag NCs as shape modulators.[51,52] In this work, we went one step further and investigated the combined effect of chloride ions and Au : Pt feeding ratios as size and shape modulators in the MW-assisted synthesis of AuPt NCs.

First, we produced NCs at different Au : Pt ratios in the absence of chloride. As is reported in Fig. 1, the size and morphology of the NCs undergo a remarkable evolution as the Au : Pt molar ratio increases. For instance, at a 0 : 1 molar ratio, small Pt NCs (3 ± 1 nm) can be observed while large Au NCs (360 ± 80 nm) are produced with a 1 : 0 ratio (Fig. 1a and i). For ratios in between, the size of the NCs increases with an ascending Au : Pt ratio. This stresses out the different reaction kinetics for both metals. In terms of shape evolution, the NCs evolve from pseudo-spheres (Fig. 1b and c) or peanut-like (Fig. 1d and e) structures at lower Au concentrations, to faceted structures such as triangles (Fig. 1f) and hexagons (Fig. 1g–i) at higher Au content. Remarkably, samples produced with a 6 : 1 ratio exhibit large NCs surrounded by smaller ones, presenting a unique homogeneous morphology (Fig. 1h). According to this observation, tuning the Au : Pt molar ratios enables the modulation of size and shape of the NCs, likely due to the variations in the nucleation kinetics of Au and Pt. We then studied the time evolution of the NCs for a 1 : 1 molar ration (Fig. S1†) observing a nucleation of small NCs already at the very beginning of the

Table 1 Summary of the structural composition and electrocatalytic performance at overpotentials @ 10 and 100 mA cm^{-2}, with Tafel slopes @ 10 mA cm^{-2}, for all the samples

Samples	Au : Pt feeding ratio	Au : Pt ICP-OES ratio	Overpotential at 10 mA cm^{-2} (mV)	Overpotential at 100 mA cm^{-2} (mV)	Tafel slope (mV dec^{-1})
Pt/C	0 : 1	0 : 1	31	72	30
Pt			28	66	19
Pt_{Cl}			29	101	33
$AuPt_{1/6}$	1 : 6	1 : 6.3	30	73	23
$AuPt_{1/6Cl}$		1 : 5.5	28	58	16
$AuPt_{1/4}$	1 : 4	1 : 3.2	32	81	26
$AuPt_{1/4Cl}$		1 : 1.6	24	51	13
$AuPt_{1/2}$	1 : 2	1 : 1.8	28	66	17
$AuPt_{1/2Cl}$		1 : 1.3	28	61	17
$AuPt_{1/1}$	1 : 1	1 : 0.7	31	102	33
$AuPt_{1/1Cl}$		1 : 0.8	39	126	47
$AuPt_{2/1}$	2 : 1	1 : 0.4	36	110	35
$AuPt_{2/1Cl}$		1 : 0.04	272	[b]	248
$AuPt_{4/1}$	4 : 1	1 : 0.1	32	114	36
$AuPt_{4/1Cl}$		1 : 0[a]	143	[b]	191
$AuPt_{6/1}$	6 : 1	1 : 0.01	200	[b]	146
$AuPt_{6/1Cl}$		1 : 0[a]	360	[b]	266
Au	1 : 0	1 : 0	311	[b]	248
Au_{Cl}			390	[b]	134

[a] No Pt detection signal due to the limit of detection of ICP-OES equipment. [b] Current densities not achieved within the applied potential range.

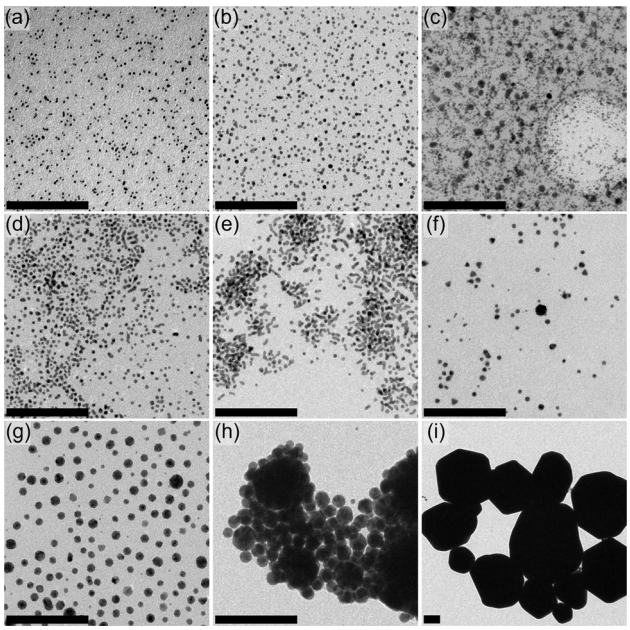

Fig. 1 TEM images of AuPt NCs produced by a MW-assisted route at 160 °C adding different Au : Pt feeding molar ratios: (a) 0 : 1 – Pt, (b) 1 : 6 – $AuPt_{1/6}$, (c) 1 : 4 – $AuPt_{1/4}$, (d) 1 : 2 – $AuPt_{1/2}$, (e) 1 : 1 – $AuPt_{1/1}$, (f) 2 : 1 – $AuPt_{2/1}$, (g) 4 : 1 – $AuPt_{4/1}$, (h) 6 : 1 – $AuPt_{6/1}$, and (i) 1 : 0 – Au. Scale bar = 100 nm.

reaction which tend to aggregate after 10 min leading to worm or peanut-like shapes.

To elucidate the influence of other synthetic parameters such as the amount of PVP_{10k} or the metal ion concentration, experiments increasing the amount of these reactants were carried out. On the one hand, the influence of the PVP_{10k} concentration in the reaction solution resulted in a varying trend depending on the Au : Pt ratio (Fig. S2†). For instance, at 1 : 0 and 0 : 1 ratios the size of the NCs remains constant despite the PVP_{10k} amount. In contrast, at intermediate ratios (1 : 4 and 1 : 1) the size of the NCs increases with increasing PVP_{10k} amount, showing a stronger effect at large Au : Pt ratios. On the other hand, when the total metal molar concentration was increased from 2 mM to 8 mM while keeping the PVP concentration constant the size of the NCs increased (Fig. S3†). For instance, for a 1 : 4 Au : Pt ratio, the size of the NCs evolve from a bimodal (5 ± 1 and 9 ± 1 nm NCs) to a monomodal distribution (6 ± 1 at 4 mM or 10 ± 2 nm) when the metal concentration (Au + Pt) was increased form 2 up to 8 mM respectively (Fig. S3a and c†). When the Au : Pt ratio was increased to 1 : 1, the NC size evolution follows a similar trend (Fig. S3d–f†). According to the above discussion, when the Au : Pt molar ratio is tuned the size can be effectively modulated from small (3 ± 1 nm at a 0 : 1 ratio) to rather large (360 ± 80 nm at 1 : 0 ratio) NCs. Conversely, the total metal molar concentration or the feeding amount of PVP_{10k} seem to have a lesser effect on the size and shape evolution.

Further characterization of the samples was carried out to elucidate the structure and composition of the AuPt NCs. For instance, XRD spectra revealed a shift in the [111] peak as the Au : Pt ratio increases (Fig. S4a†), which agrees with the increasing content of Au in a Pt structure. UV-vis spectra also demonstrated an evolution of the absorption with the increasing molar amount of Au. The deviation of the local surface plasmon resonance (LSPR) from its reported value for Au NCs (530 nm) is attributed to a size and composition evolution of the samples (Fig. S4b†).[53] For 2 : 1 and 4 : 1 ratio, this peak was located slightly below 530 nm which is consistent

with the presence of Pt atoms inside a Au NCs.[54] For higher Au concentrations (*i.e.*, 6 : 1 and 1 : 0), the red-shift of the LSPR was attributed to the presence of larger NCs.[55]

After this initial analysis, AuPt NCs were produced following the same procedure as the previously presented samples, but with the addition of a controlled amount of chloride in the solution (Fig. 2). Despite this new set of NCs showed an increase in size with an increasing amount of Au too, the evolution of size and shape was remarkably different. For instance, from 0 : 1 to 1 : 2 ratios (Pt_{Cl} to $AuPt_{1/2Cl}$, Fig. 2a–d), shapes evolve from elongated or pod-like structures to nanoclusters with sizes ranging from 5 ± 1 to 14 ± 2 nm. These sizes are larger than those observed for NCs produced with the same Au : Pt ratio but without chloride (Fig. 1a–d). Noteworthy, we observed that samples synthesized in the presence of chloride resemble those produced without chloride but at higher Au : Pt ratios. For example, the samples produced at 1 : 2, 1 : 1, and 2 : 1 Au : Pt ratios in the presence of chloride (Fig. 2d–f, respectively) resemble those produced at 2 : 1, 4 : 1 and 6 : 1 without chloride (Fig. 1f–h, respectively). This observation suggests a modulation of the nucleation kinetics mediated by chloride, likely due to the different interaction or coordination of chloride with Au and Pt ions. This point will be discussed further below.

The final concentration of Au and Pt within the NCs was studied through ICP-OES analysis (Table 1 and Fig. S5†). For small Au : Pt feeding ratios, the stoichiometry of the NCs agree with the initial metal feeding ratios for samples produced without addition of chloride. Increasing the Au : Pt ratio up to 1 : 1 show a deviation of the stoichiometry of the NCs compared to the feeding ratio but remain within reasonable agreement. However, for ratios above 1 : 1 the amount of Pt is smaller than the initial metal feeding. For instance, at 2 : 1 and 6 : 1 Au : Pt feeding ratios the, NCs stoichiometry is 1 : 0.4 and 1 : 0.01, respectively. In the presence of chloride this deviation trend between NC's stoichiometry and the feeding ratio appears to be clearly enhanced, in particular above the 1 : 1 ratio. Indeed, for 4 : 1 or 6 : 1 the values for Pt content are below the ICP-OES detection limit, thus indicating a decrease or delay in the Pt nucleation. From these data, we concluded that a high amount of Au strongly modulates Pt nucleation and growth kinetics, inhibiting its nucleation at large concentrations of Au (or low concentrations of Pt). This effect is enhanced when chloride was added to the reaction solution as the Au : Pt ratios of 2 : 1, 4 : 1, and 6 : 1 show a one-order-of-magnitude difference between samples produced with or without chloride. This led us to hypothesize the initial formation of chloride-stabilized metal clusters that modulate the reaction kinetics. To be specific, promoting the formation of more stable Pt clusters as compared to Au ones. This would delay nucleation favoring the reduction of Pt on top of an already-formed Au core when chloride is present in solution. Finally, the XRD peak positions evolves with increasing content of Au precursor (Fig. S4c†). The (111) peak position of the Pt structure (Pt_{Cl} sample) shifts to lower angles for sample $AuPt_{1/6Cl}$ to $AuPt_{1/1Cl}$, thus indicating the possible formation of an AuPt alloy. Noteworthy, for higher Au content ($AuPt_{2/1Cl}$), the XRD peaks fit to an Au structure indicating the formation of an Au core. A similar trend was observed for the evolution of the LSPR (Fig. S4d†).

To investigate further the modulation by chloride in the nucleation-growth process, several volumes of a HCl solution (0, 10, 20 and 50 μL) were introduced into a reaction solution containing different Au : Pt ratios (0 : 1, 1 : 4, 1 : 1 and 1 : 0, Fig. S6†). As a general trend, we observed that increasing chloride ions lead to an increase in the NCs size, which is consistent with a delayed or inhibited nucleation mediated by chloride-stabilized metal clusters (Fig. S6a–l†). However, when only Au was present in the solution, the size of the NCs decreased with increasing chloride concentration (Fig. S6m–q†). This highlights the opposite effect of chloride on both metal atoms; Au and Pt. In that context, adding chloride ions in the reaction solution likely promotes the formation of Au intermediates that favor nucleation against growth, thus leading to a controlled formation of NCs.[56] As for Pt, controlled conditions are likely already achieved without the addition of chloride. Consequently, an excess of chloride induces a delayed nucleation for Pt contributing to the formation of larger NCs or the reduction of Pt on top of the Au metal core. Overall, the differences in the final composition of NCs reported in Table 1 for samples produced under the same conditions but with varying chloride ion concentrations align with the above discussion. It is worth mentioning that the stabilization of metal clusters or complexes mediated by chloride is compatible with the reported etching effect of halides in metal NCs, particularly for Ag nanocubes.[49] This suggests the nucleation and dissolution of Pt atoms during the reaction, particularly on top of Au cores, which would

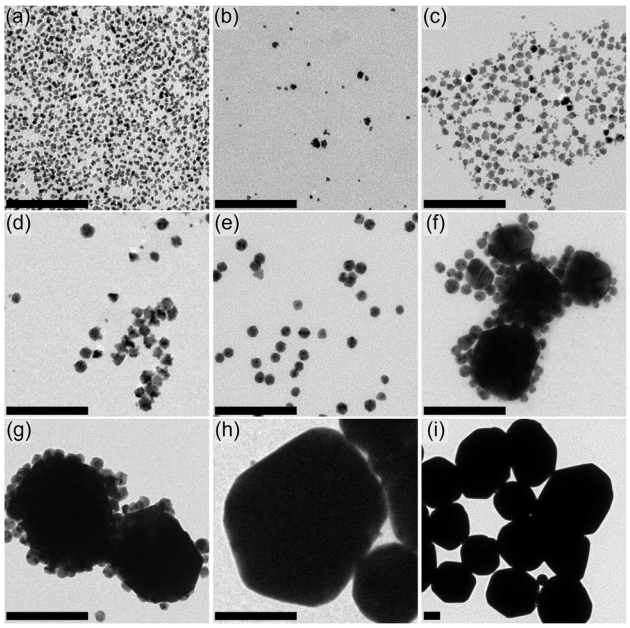

Fig. 2 TEM images showing the size and shape evolution of AuPt NCs produced by adding a controlled amount of chloride with different Au : Pt ratios: (a) 0 : 1 – Pt_{Cl}, (b) 1 : 6 – $AuPt_{1/6Cl}$, (c) 1 : 4 – $AuPt_{1/4Cl}$, (d) 1 : 2 – $AuPt_{1/2Cl}$, (e) 1 : 1 – $AuPt_{1/1Cl}$, (f) 2 : 1 – $AuPt_{2/1Cl}$, (g) 4 : 1 – $AuPt_{4/1Cl}$, (h) 6 : 1 – $AuPt_{6/1Cl}$, and (i) 1 : 0 – Au_{Cl}. Scale bar = 100 nm.

explain the absence of Pt under certain conditions tested in this work.

We also conducted experiments to explore the influence of different amounts of PVP and increasing metal concentration at a fixed chloride concentration (Fig. S7 and S8†). Similar to the samples synthesized in the absence of chloride ions, excess of PVP has a strong influence in size and shape at higher Au concentrations (*e.g.*, 1 : 1 and 1 : 0). In this regard, increasing amounts of PVP showed a stronger effect in the nucleation kinetics in the presence of chloride ions. In particular, a bimodal size distribution or bigger Au NCs were obtained at a 1 : 1 or 1 : 0 ratios, respectively (Fig. S7g–l†). This observation could be attributed to a potential interplay or competition between PVP and chloride ions, further modifying the reaction kinetics. The effect of increasing metal concertation is enhanced in the presence of additional chloride ions (Fig. S8†). In detail, an increasing concentration of metal ions in solution (from 2 mM to 4 or 8 mM) lead to a defocusing of the size distribution, observing a bimodal distribution where small NCs surround larger ones. This observation corroborates the strong correlation between the amount of chloride and the different nucleation kinetics for each metal. Finally, we sought to validate the influence of MW radiation on the experimental outcomes by comparing our samples with those produced under the same synthesis conditions but using conventional oil bath heating (Fig. S9†). For the 1 : 1 Au : Pt ratio, samples prepared both without and with the addition of chloride revealed significant disparities between both heating approaches. In particular, conventional oil bath heating resulted in larger NCs prone to nucleate in a bimodal size distribution. Finally, the benefits of the MW-assisted approach were confirmed by a high reproducibility and potential scalability (see Fig. S10†).

The electrocatalytic performance of the samples was tested by LSV measurements in an Ar-saturated aqueous solution (0.5 M H_2SO_4). Before running the LSV curves, the PVP_{10k} coating was removed to achieve the maximum availability of active sites on the surface.[57] PVP_{10k} removal was monitored by FT-IR measurements, confirming the absence of the three characteristic peaks for PVP_{10k} (1283 cm^{-1} for C–N stretching; 1422 cm^{-1} for C–H bending and 1656 cm^{-1} for C=O stretching, Fig. S11†). As depicted in Fig. 3 and Table 1, samples synthesized under standard conditions generally show increasing overpotentials as the amount of Au increases in the NCs (Fig. 3a and b). Indeed, samples with the highest Au content ($Au_{6/1}$ and $Au_{1/0}$) likely suffer from a higher hydrogen-adsorption-free energy associated with Au, resulting in poor activities.[58] When the amount of Pt increases inside the NCs, the overpotentials are similar to the one for commercial Pt/C catalyst (31 mV at 10 mA cm^{-2}). For instance, samples produced with ratios ranging from 0 : 1 to 1 : 1 show overpotentials between 28 and 32 mV at 10 mA cm^{-2}. Nevertheless, at higher current densities up to 100 mA cm^{-2}, some of the AuPt samples exhibit lower or higher values (66 or 102 mV) than commercial Pt/C (72 mV). A similar trend is observed when analyzing the slope of the Tafel plots (Fig. 3c and Table 1). In particular, $AuPt_{1/2}$, $AuPt_{1/4}$, and $AuPt_{1/6}$ samples display slopes of 17, 26, and 23 mV dec^{-1}, respectively, notably below that of commercial Pt/C (30 mV dec^{-1}). Overall, when no additional chloride is added to the reaction solution, the highest performance is achieved for the $AuPt_{1/2}$ sample, which owns a 1 : 1.8 Au : Pt ratio according to ICP-OES measurements (Table 1). Noteworthy, this result demonstrates that the activity is not directly related to the amount of Pt content.

The same electrochemical characterization was carried out for the set of samples produced in the presence of an excess of chloride ions (Fig. 3d–f). In this case, the evolution of the overpotentials as a function of the Pt content in the NCs shows a parabolic behavior, particularly for overpotentials measured at 100 mA cm^{-2}. Furthermore, within the composition range of 1 : 6 to 1 : 2 Au : Pt ratio, the electrocatalytic activity is enhanced compared to samples produced under standard conditions, without the addition of chlorine. In that range, a clear minimum is observed for the $AuPt_{1/4Cl}$ sample, which has a final Pt content of *ca.* 62% (1 : 1.63 Au : Pt ratio) and shows overpotentials of 24 and 51 mV at 10 and 100 mA cm^{-2}, respectively. It is worth mentioning that these values are below those measured for commercial Pt/C catalysts (31 and 72 mV at 10 and 100 mA cm^{-2}, respectively). Worth mentioning, the overpotentials are similar or even slightly higher when chloride is added for the rest of the samples. As discussed previously, the addition of chloride not only modifies the final Au : Pt content, but also promotes the formation of larger NCs. According to the general theory, larger NCs should lead to a lower activity due to the loss of active sites on the surface, as reflected in Pt and Pt_{Cl} samples (66 and 101 mV at 100 mA cm^{-2}, respectively). Nevertheless, when comparing samples produced with or without chloride in the range from 1 : 6 to 1 : 2 Au : Pt ratio, lower overpotentials are observed when chloride is added despite the larger NCs. The same effect is observed for the Tafel slopes (β), observing lower slopes in the same range (*i.e.*, 1 : 6 to 1 : 2 Au : Pt ratio) when NCs were produced using an excess of chloride. Even more interestingly, the $AuPt_{1/4Cl}$ sample demonstrates the best electrocatalytic activity towards HER despite having a lower Pt content than $AuPt_{1/6Cl}$. Notably, the $AuPt_{1/4Cl}$ and $AuPt_{1/2}$ ratios are closely aligned (1 : 1.63 and 1 : 1.76, respectively). However, their respective performance disparities highlight that catalytic activity is not solely determined by Pt content. A straightforward comparison of the reported values for the Tafel slope and overpotentials in the literature highlights the outstanding performance observed for our $AuPt_{1/4Cl}$ NCs (Fig. 3g). Finally, the performances measured for Pt and Pt_{Cl} samples were similar to the values measured for a commercial Pt/C catalyst.

Regarding the enhancement of electrocatalytic activities, the observed improvement after the addition of chloride is likely attributed to the formation of a Au–Pt structure rather than a simple AuPt alloy. This structure appears to provide higher Pt exposure to the environment. To explore this hypothesis, HR-STEM and EDX mapping were performed on both $AuPt_{1/4}$ and $AuPt_{1/4Cl}$ samples (Fig. 4). Noteworthy, HR-HAADF images of $AuPt_{1/4}$ NCs exhibit a homogeneous crystallinity, indicating an even distribution of Au and Pt atoms along the NCs (as seen in Fig. 4a). In addition, EDX mapping confirms that the Pt signal is slightly higher than that of Au in all the AuPt NCs, as shown in

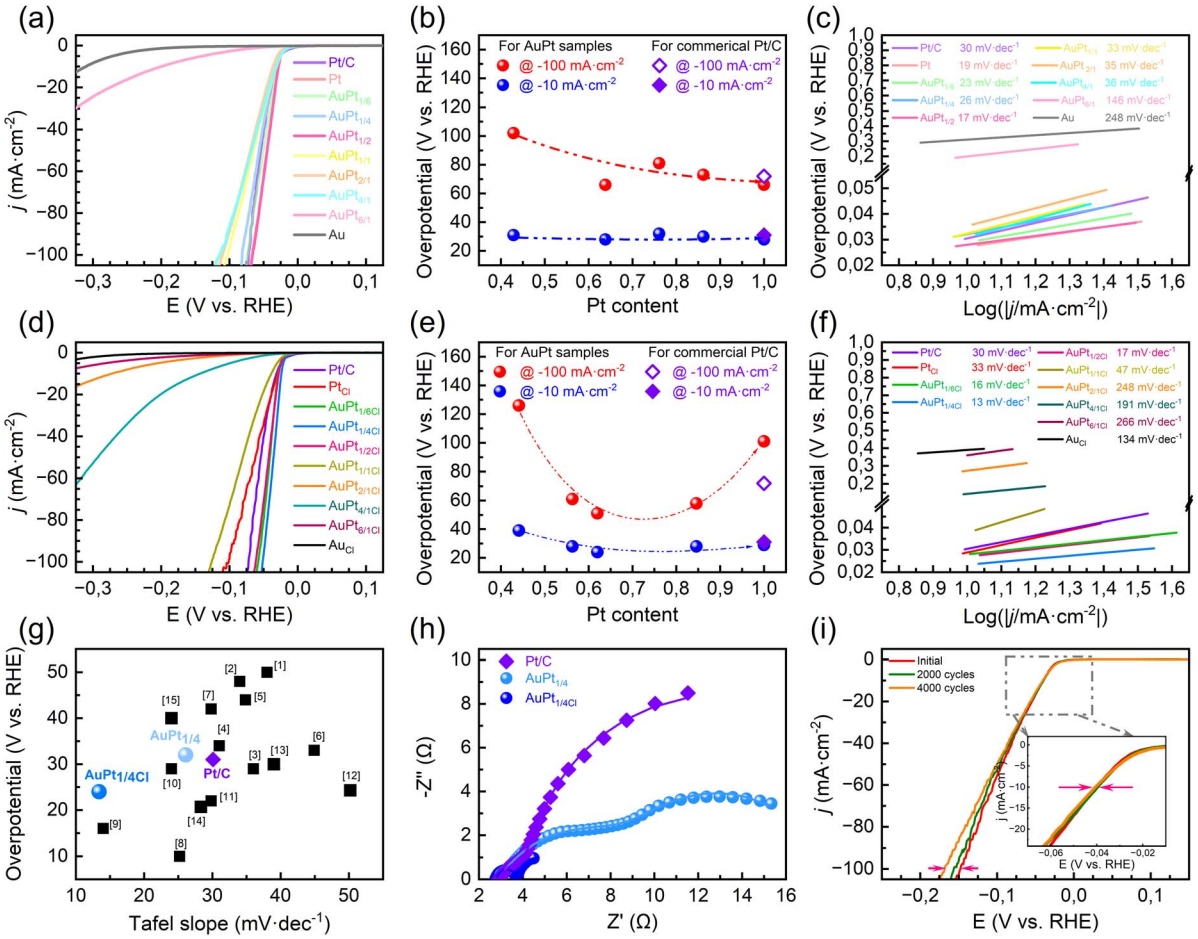

Fig. 3 Electrocatalytic HER performance in 0.5 M H_2SO_4. (a) LSV, (b) overpotentials *vs.* Pt content, and (c) Tafel slope of the AuPt NCs synthesized in the absence of chloride, respectively. (d) LSV, (e) overpotentials *vs.* Pt content, and (f) Tafel slope of the set of AuPt NCs synthesized in the presence of chloride, respectively. (g) Overpotential *vs.* Tafel slope plot for commercial Pt/C, $AuPt_{1/4}$, and $AuPt_{1/4Cl}$ samples. Data are compared with reported values of state-of-the-art electrocatalysts based on Pt alloys (references are listed in Table S1†). (h) EIS Nyquist plot for commercial Pt/C, $AuPt_{1/4}$, and $AuPt_{1/4Cl}$. (i) Evolution of the stability of $AuPt_{1/4Cl}$ by running CV for 2000 and 4000 cycles, respectively.

Fig. 4b, consistent with the Au : Pt ratio measured by ICP-OES (1 : 3.19, as detailed in Table 1). In contrast, HR-HAADF images acquired from $AuPt_{1/4Cl}$ NCs reveal a non-homogeneous contrast, particularly noticeable as blurred contrast in the core of the NC, as shown in Fig. 4c. Elemental EDX mapping further illustrates a core–shell structure wherein a Pt shell surrounds an Au core (Fig. 4d). This observation corroborates the influence of chloride in modulating the Au and Pt nucleation/growth kinetics, favoring the nucleation of the Au core while limiting the nucleation of Pt atoms onto its surface. Some works have featured the selective binding of halide ions to different metals and the formation of various metal complexes and clusters with different reaction kinetics.[59] This could elucidate preferential nucleation and subsequent stabilization of Au cores over Pt ones. This hypothesis is further supported by the observation of a lower Pt content in $AuPt_{1/4Cl}$ compared to $AuPt_{1/4}$ (1 : 1.63 and 1 : 3.19 respectively, Table 1). Accordingly, the higher efficiency of $AuPt_{1/4Cl}$ is unequivocally attributed to a rational distribution of the Pt atoms on the Au core's surface. This configuration not only maximizes the exposure of Pt atoms to the environment but also prevents Au atoms from interacting with the environment, thereby reducing the contribution of low-performing Au atoms to HER. Despite that, it is essential to note that this should not impede the contribution of the electron cloud of the Au core to the electrocatalytic activity pointing towards a synergetic effect. However, this hypothesis requires further investigation beyond the scope of this work.

The calculation of the electrochemical active surface area (ECSA) of the three samples (Pt/C, $AuPt_{1/4}$, and $AuPt_{1/4Cl}$) by applying CV curves at different scan rates in the non-faradaic region (Fig. 5a) demonstrates that the core–shell heterostructure maximizes the available active Pt atoms. According to the slopes, commercial Pt/C exhibits the highest slope (1.46 mF cm^{-2}), while $AuPt_{1/4}$ and $AuPt_{1/4Cl}$ show lower slope values (0.42 and 1.18 mF cm^{-2}, respectively) resulting in higher ECSA for Pt/C (41.7 $m^2\ g^{-1}$) compared to $AuPt_{1/4}$ and $AuPt_{1/4Cl}$ (12.0 and 33.7 $m^2\ g^{-1}$, respectively). The commercial Pt/C catalyst contains a 20 wt% Pt content, whereas $AuPt_{1/4}$ and $AuPt_{1/4Cl}$ have 8.4 and 6.9 wt% Pt content. Despite the higher number of active sites for commercial Pt/C compared to AuPt samples, its overpotential is

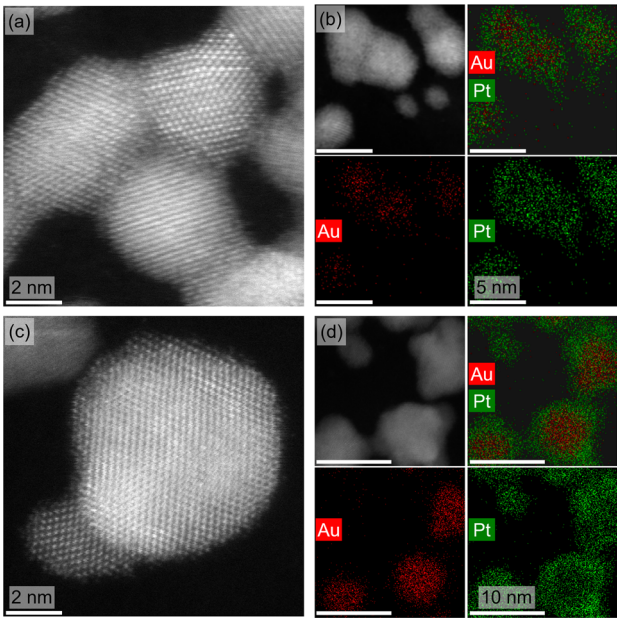

Fig. 4 High-resolution HAAFD-STEM images and EDX elemental mapping of $AuPt_{1/4}$ (a and b) and $AuPt_{1/4Cl}$ (c and d). Au and Pt elements are displayed as red and green colours, respectively.

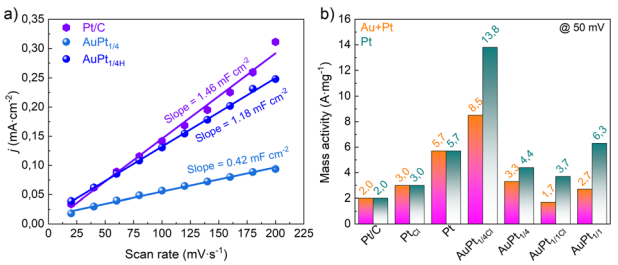

Fig. 5 (a) Calculation of the electrochemical double layer capacitance (C_{dl}) for commercial Pt/C, $AuPt_{1/4}$, and $AuPt_{1/4Cl}$ (see Fig. S15†) (b) mass activities of commercial Pt/C, $AuPt_{1/1}$, $AuPt_{1/1Cl}$, $AuPt_{1/4}$, and $AuPt_{1/4Cl}$, Pt, and Pt_{Cl} at the overpotential of 50 mV with the same total loading on the working electrode.

still higher so indicating that the activity is not only related to the ECSA but other parameters promoting the reaction. To further analyze the intrinsic activity of these electrocatalysts, their mass activity (normalized by the Pt mass) was calculated at 50 mV (Fig. 5b). Noteworthy, the mass activity of the $AuPt_{1/4Cl}$ is 13.8 A mg_{Pt}^{-1}, which is almost 6.9 times higher than that of commercial Pt/C (2.0 A mg_{Pt}^{-1}), and around 3.1 times of $AuPt_{1/4}$ (4.4 A mg_{Pt}^{-1}). Therefore, arranging Pt atoms on top of a Au core likely enhances its activity while promoting interactions with the core that significantly improved the overall HER electrocatalytic performance. Certainly, when considering the total mass of the NCs (Au + Pt) these values are slightly low. For instance, 8.5 A mg^{-1} for the $AuPt_{1/4Cl}$ sample (Fig. 5b) which represents a 4.25 fold enhancement compared to Pt/C.

To gain a better insight into the kinetic mechanism governing the HER, EIS characterization was performed on commercial Pt/C, $AuPt_{1/4}$, and $AuPt_{1/4Cl}$ samples (Fig. 3h and S13†). The estimated solution resistance (R_s) observed from the Nyquist plots is similar for all samples and in the order of 2.8 to 2.9 Ω at −13 mV (Table S2†). In this case, the semicircles can be attributed to two interfaces associated with the adsorption of species (mainly H^+, first semicircle R_1) and the electron transfer (second semicircle R_2).[60] When comparing the R_1 values for the three samples, the $AuPt_{1/4Cl}$ shows the lowest value (0.87 Ω) compared to the values for $AuPt_{1/4}$ and commercial Pt/C (6.34 and 1.54 Ω, respectively). By comparing the resistance corresponding to the transfer of electrons (R_2), $AuPt_{1/4Cl}$ shows again the lowest values (2.4 Ω) compared to the ones measured for $AuPt_{1/4}$ and Pt/C (9.24 and 17.04 Ω, respectively). This indicates efficient species adsorption and rapid charge transfer in $AuPt_{1/4Cl}$. To corroborate our hypothesis, we ran HER measurements in neutral (1 M potassium phosphate-buffered saline, PBS, pH = 7) and alkaline (1 M potassium hydroxide, pH = 14) media. As shown in Fig. S14,† in neutral and alkaline solutions, $AuPt_{1/4}$ and $AuPt_{1/4Cl}$ exhibited poorer performance than commercial Pt/C. Remarkably, $AuPt_{1/4Cl}$ exhibits the highest overpotential at 10 mA cm^{-2} in alkaline media, while $AuPt_{1/4}$ showed a better activity close to the one measured for commercial Pt/C (Table S3†). This observation proves the crucial role of H^+ adsorption in the HER performance of AuPt structures and, at the same time, the synergetic effect differences that Au and Pt could play in alkaline media. The significant improvement of the $AuPt_{1/4}$ NCs from neutral to alkaline media could result from the higher adsorption energy of H^+ species in Au, thus leading to an improved activity at higher pH.

Finally, the stability of the $AuPt_{1/4Cl}$ electrocatalyst was evaluated by conducting 2000 and 4000 cycles of CV (Fig. 3i) and a chronopotentiometry test (Fig. S16†). As observed, the overpotential at 10 mA cm^{-2} does not undergo significant increases, remaining close to 30 mV after 2000 or even 4000 cycles, as shown in the inset image of Fig. 3i. A slight deviation is observed in the overpotentials at 100 mA cm^{-2}, with an increase from 148 mV to 156 mV and 168 mV for 2000 and 4000 cycles, respectively. Nevertheless, the activity of the $AuPt_{1/4Cl}$ electrocatalyst remains relatively stable after 4000 cycles. The chronoamperometry test was carried out by drop casting a catalyst ink containing $AuPt_{1/4Cl}$ NCs onto a carbon cloth (1 × 1.25 cm^2). Chronopotentiometry was run over 200 hours in an H-type cell maintaining a constant current density of 10 mA cm^{-2} (Fig. S16†). Samples show rather good stability with an increase of the overpotential of *ca.* 5–6% after 200 hours. These results are consistent with the trend observed in Fig. 3i and comparable with the reported stabilities for other catalyst (Table S4†), indicating a good stability of $AuPt_{1/4Cl}$ performance over prolonged operating time. Analysis of the sample after the long stability test confirmed that the structure of a Au-rich core surrounded by a Pt shell was preserved (Fig. S17†). Noteworthy, X-ray photoelectron spectroscopy (XPS) analysis confirmed a partial oxidation of the Pt-shell as well as an increase in the Au^{1+} contribution after 200 hours (Fig. S18†). This increase could be related to a partial migration of Au atoms to the surface that eventually does reduce the catalytic activity. Indeed, this hypothesis is in line with the *ca.* 25% increase of the

overpotential after 12 hours when the current was increased to 50 mA cm^{-2} (Fig. S16†).

4 Conclusions

In summary, we have successfully synthesized a series of AuPt NCs with varying Au : Pt ratios using a fast and facile MW-assisted synthetic approach. The addition of HCl played a pivotal role providing precise control over the structure and morphology of the NCs. Ultimately, $AuPt_{1/4Cl}$ was identified as the most promising candidate for the HER in acidic media demonstrating remarkable electrocatalytic activity despite not having the highest Pt content among all the samples. Precisely, it exhibited overpotentials of 24 mV and 51 mV (at 10 and 100 mA cm^{-2}, respectively) and a Tafel slope of 13 mV dec^{-1}. This excellent performance can be attributed to the distinctive core–shell structure of NCs, wherein a Pt shell wraps the Au core. This configuration maximizes the exposure of Pt atoms to the surrounding environment, surpassing the activity of commercial Pt/C catalysts. Furthermore, synergistic effects between the Au core and the Pt shell likely contribute to superior performance by modulating the electronic structure of the core–shell nanocatalyst. Despite its low Pt content, the $AuPt_{1/4Cl}$ nanocatalyst exhibited a hydrogen production rate significantly higher than that of commercial Pt/C (by 4.25 fold) and surpassed the $AuPt_{1/4}$ counterpart (by 2.6 fold). In this context, the low Pt content combined with the high hydrogen production rate offsets the presence of Au in the NCs. Future research should focus on replacing Au with more cost-effective and abundant elements such as Ag, Ni, Co, or Cu. These findings underscore the successful integration of MW-assisted synthesis and halide ions for the rational design of low-Pt content electrocatalysts with enhanced performance in HER.

Data availability

The data supporting this article have been included as part of the ESI.†

Author contributions

Xuesong Zhang: conceptualization, data curation, formal analysis, investigation, methodology, writing-original draft, writing-review & editing. Jesús Chacón-Borrero: data curation, formal analysis, investigation. Ren He: formal analysis, investigation. Jaume Gázquez: formal analysis, methodology. Miquel Torras: conceptualization, investigation. Andreu Cabot: conceptualization, writing-review & editing. Anna Roig: funding acquisition, investigation, writing-review & editing. Pablo Guardia: conceptualization, data curation, formal analysis, funding acquisition, investigation, methodology, project administration, supervision, writing-original draft, writing-review & editing.

Conflicts of interest

The authors declare no conflict of interest.

Acknowledgements

This work was financially supported by the MCIN/AEI/10.13039/501100011033 (Grant No. CNS2022-135583 and PID2021-122645OB-I00), the Generalitat de Catalunya (AGAUR Grant No. LLAV 00096 and 2017SGR765), and the 'Severo Ochoa' Programme for Center of Excellence in R&D funded by MCIN and by FEDER, "A way of making Europe" (Grant No. CEX2023-001263-S). P. G. acknowledges financial support from the Ramon y Cajal program funded by the MCIN/AEI/10.13039/501100011033 and the "FSE invierte en tu futuro" (Grant No. RYC2019-028414). X. Z. and J. C.-B. are enrolled in the Materials Science PhD program of the UAB. X. Z. acknowledges financial support from the Chinese Scholarship Council (Grant No. 202106650006). Authors acknowledge the use of instrumentation as well as the technical advice provided by the National Facility ELECMI ICTS, node "Laboratorio de Microscopias Avanzadas (LMA)" at "Universidad de Zaragoza".

References

1 F. Ueckerdt, C. Bauer, A. Dirnaichner, J. Everall, R. Sacchi and G. Luderer, *Nat. Clim. Change*, 2021, **11**(5), 384–393.
2 P. Nikolaidis and A. Poullikkas, *Renew. Sustain. Energy Rev.*, 2017, **67**, 597–611.
3 C. Xu, M. Zhang, X. Yin, Q. Gao, S. Jiang, J. Cheng, X. Kong, B. Liu and H. Q. Peng, *J. Mater. Chem. A*, 2023, **11**, 18502–18529.
4 M. Chatenet, B. G. Pollet, D. R. Dekel, F. Dionigi, J. Deseure, P. Millet, R. D. Braatz, M. Z. Bazant, M. Eikerling, I. Staffell, P. Balcombe, Y. Shao-Horn and H. Schäfer, *Chem. Soc. Rev.*, 2022, **51**, 4583–4762.
5 Y. Luo, Z. Zhang, M. Chhowalla and B. Liu, *Adv. Mater.*, 2022, **34**, 1–18.
6 W. A. Saidi, T. Nandi and T. Yang, *Electrochem. Sci. Adv.*, 2023, **3**, e2100224.
7 S. Pan, H. Li, D. Liu, R. Huang, X. Pan, D. Ren, J. Li, M. Shakouri, Q. Zhang, M. Wang, C. Wei, L. Mai, B. Zhang, Y. Zhao, Z. Wang, M. Graetzel and X. Zhang, *Nat. Commun.*, 2022, **13**, 2294.
8 J. Zhao, N. Liao and J. Luo, *J. Mater. Chem. A*, 2023, **11**, 9682–9690.
9 F. Liu, C. Shi, X. Guo, Z. He, L. Pan, Z. Huang, X. Zhang and J. Zou, *Adv. Sci.*, 2022, **9**, 2200307.
10 M. Herbaut, M. Siaj and J. P. Claverie, *ACS Appl. Nano Mater.*, 2021, **4**, 907–910.
11 L. Jiao and H. L. Jiang, *Chin. J. Catal.*, 2023, **45**, 1–5.
12 Y. Li, Y. Sun, Y. Qin, W. Zhang, L. Wang, M. Luo, H. Yang and S. Guo, *Adv. Energy Mater.*, 2020, **10**, 1–20.
13 I. T. McCrum and M. T. M. Koper, *Nat. Energy*, 2020, **5**, 891–899.
14 S. Zhu, X. Qin, F. Xiao, S. Yang, Y. Xu, Z. Tan, J. Li, J. Yan, Q. Chen, M. Chen and M. Shao, *Nat. Catal.*, 2021, **4**, 711–718.
15 J. Tymoczko, F. Calle-Vallejo, W. Schuhmann and A. S. Bandarenka, *Nat. Commun.*, 2016, **7**, 10990.
16 Y. Nakaya and S. Furukawa, *Chem. Rev.*, 2023, **123**, 5859–5947.

17 J. Liu, C. Lee, Y. Hu, Z. Liang, R. Ji, X. Y. D. Soo, Q. Zhu and Q. Yan, *SmartMat*, 2023, **4**, e1210.
18 Y. Shi, Z. R. Ma, Y. Y. Xiao, Y. C. Yin, W. M. Huang, Z. C. Huang, Y. Z. Zheng, F. Y. Mu, R. Huang, G. Y. Shi, Y. Y. Sun, X. H. Xia and W. Chen, *Nat. Commun.*, 2021, **12**(1), 1–11.
19 Z. Zeng, S. Kuang, Z. F. Huang, X. Chen, Y. Su, Y. Wang, S. Zhang and X. Ma, *Chem. Eng. J.*, 2022, **433**, 134446.
20 R. Q. Yao, Y. T. Zhou, H. Shi, W. Bin Wan, Q. H. Zhang, L. Gu, Y. F. Zhu, Z. Wen, X. Y. Lang and Q. Jiang, *Adv. Funct. Mater.*, 2021, **31**, 2009613.
21 D. Strmcnik, M. Uchimura, C. Wang, R. Subbaraman, N. Danilovic, D. Van Der Vliet, A. P. Paulikas, V. R. Stamenkovic and N. M. Markovic, *Nat. Chem.*, 2013, **5**(4), 300–306.
22 C. Lim, A. R. Fairhurst, B. J. Ransom, D. Haering and V. R. Stamenkovic, *ACS Catal.*, 2023, **13**, 14874–14893.
23 N. S. Porter, H. Wu, Z. Quan and J. Fang, *Acc. Chem. Res.*, 2013, **46**, 1867–1877.
24 G. Gao, G. Zhu, X. Chen, Z. Sun and A. Cabot, *ACS Nano*, 2023, **17**, 20804–20824.
25 Y. Lu, K. Huang, X. Cao, L. Zhang, T. Wang, D. Peng, B. Zhang, Z. Liu, J. Wu, Y. Zhang, C. Chen and Y. Huang, *Adv. Funct. Mater.*, 2022, **32**, 2110645.
26 S. Deng, B. Zhang, P. Choo, P. J. M. Smeets and T. W. Odom, *Nano Lett.*, 2021, **21**, 1523–1529.
27 Y. Chen, H. Sun, B. C. Gates, Y. Chen, H. Sun and B. C. Gates, *Small*, 2021, **17**, 2004665.
28 K. L. Zhou, Z. Wang, C. B. Han, X. Ke, C. Wang, Y. Jin, Q. Zhang, J. Liu, H. Wang and H. Yan, *Nat. Commun.*, 2021, **12**(1), 1–10.
29 W. Geng, X. Song, Z. Wei, M. Cao and R. Cao, *ACS Appl. Energy Mater.*, 2022, **5**, 15597–15604.
30 Z. X. Ge, Y. Ding, T. J. Wang, F. Shi, P. J. Jin, P. Chen, B. He, S. B. Yin and Y. Chen, *J. Energy Chem.*, 2023, **77**, 209–216.
31 K. Loza, M. Heggen and M. Epple, *Adv. Funct. Mater.*, 2020, **30**, 1909260.
32 P. Lu, J. Zhou, Y. Hu, J. Yin, Y. Wang, J. Yu, Y. Ma, Z. Zhu, Z. Zeng and Z. Fan, *J. Mater. Chem. A*, 2021, **9**, 19025–19053.
33 D. Strmcnik, P. P. Lopes, B. Genorio, V. R. Stamenkovic and N. M. Markovic, *Nano Energy*, 2016, **29**, 29–36.
34 S. Tanaka, N. Hoshi and M. Nakamura, *ChemElectroChem*, 2023, **10**, e202300095.
35 D. Mott, J. Luo, P. N. Njoki, Y. Lin, L. Wang and C. J. Zhong, *Catal. Today*, 2007, **122**, 378–385.
36 P. P. Lopes, D. Li, H. Lv, C. Wang, D. Tripkovic, Y. Zhu, R. Schimmenti, H. Daimon, Y. Kang, J. Snyder, N. Becknell, K. L. More, D. Strmcnik, N. M. Markovic, M. Mavrikakis and V. R. Stamenkovic, *Nat. Mater.*, 2020, **19**, 1207–1214.
37 Y. Yu, S. J. Lee, J. Theerthagiri, Y. Lee and M. Y. Choi, *Appl. Catal., B*, 2022, **316**, 121603.
38 Y. Cao, Y. Xiahou, L. Xing, X. Zhang, H. Li, C. S. Wu and H. Xia, *Nanoscale*, 2020, **12**, 20456–20466.
39 X. Wang, J. Qi, X. Luo, Z. Yang, Y. Fan, Z. Jiang, C. Liu, J. Yang and W. Chen, *Int. J. Hydrogen Energy*, 2021, **46**, 36771–36780.
40 R. Wan, M. Luo, J. Wen, S. Liu, X. Kang and Y. Tian, *J. Energy Chem.*, 2022, **69**, 44–53.
41 L. D. Germano, V. S. Marangoni, N. V. V. Mogili, L. Seixas and C. M. Maroneze, *ACS Appl. Mater. Interfaces*, 2019, **11**, 5661–5667.
42 M. Torras and A. Roig, *ACS Omega*, 2020, **5**, 5731–5738.
43 M. Torras and A. Roig, *Cryst. Growth Des.*, 2021, **21**, 5027–5035.
44 J. Seth and B. L. V. Prasad, *Nano Res.*, 2016, **9**, 2007–2017.
45 X. Huang, Y. Li, Y. Li, H. Zhou, X. Duan and Y. Huang, *Nano Lett.*, 2012, **12**, 4265–4270.
46 S. E. Lohse, N. D. Burrows, L. Scarabelli, L. M. Liz-Marzán and C. J. Murphy, *Chem. Mater.*, 2014, **26**, 34–43.
47 P. Guardia, S. Nitti, M. E. Materia, G. Pugliese, N. Yaacoub, J. M. Greneche, C. Lefevre, L. Manna and T. Pellegrino, *J. Mater. Chem. B*, 2017, **5**, 4587–4594.
48 J. Lim, W. K. Bae, K. U. Park, L. Z. Borg, R. Zentel, S. Lee and K. Char, *Chem. Mater.*, 2013, **25**, 1443–1449.
49 S. Ghosh and L. Manna, *Chem. Rev.*, 2018, **118**, 7804–7864.
50 X. Zhang, B. Liu, C. Hu, S. Chen, X. Liu, J. Liu, F. Chen, J. Chen and F. Xie, *Spectrochim. Acta, Part A*, 2020, **228**, 117733.
51 P. C. Chen, M. Liu, J. S. Du, B. Meckes, S. Wang, H. Lin, V. P. Dravid, C. Wolverton and C. A. Mirkin, *Science*, 2019, **363**, 959–964.
52 Q. Wang, W. Jia, B. Liu, W. Zhao, C. Li, J. Zhang and G. Xu, *Chem.–Asian J.*, 2012, **7**, 2258–2267.
53 V. Coviello, D. Forrer and V. Amendola, *ChemPhysChem*, 2022, **23**, e202200136.
54 V. Amendola, R. Pilot, M. Frasconi, O. M. Maragò and M. A. Iatì, *J. Phys.: Condens. Matter*, 2017, **29**, 203002.
55 J. Rodríguez-Fernández, J. Pérez-Juste, F. J. G. De Abajo and L. M. Liz-Marzán, *Langmuir*, 2006, **22**, 7007–7010.
56 A. Loiudice and R. Buonsanti, *Nat. Synth.*, 2022, **1**(5), 344–351.
57 Q. Fan, K. Liu, Z. Liu, H. Liu, L. Zhang, P. Zhong, C. Gao, Q. Fan, K. Liu, Z. Liu, H. Liu, L. Zhang, P. Zhong and C. Gao, *Part. Part. Syst. Charact.*, 2017, **34**, 1700075.
58 Z. W. She, J. Kibsgaard, C. F. Dickens, I. Chorkendorff, J. K. Nørskov and T. F. Jaramillo, *Science*, 2017, **355**, eaad4998.
59 J. Choi, Y. Lee, J. Kim and H. Lee, *J. Power Sources*, 2016, **307**, 883–890.
60 Y. Guo, B. Hou, X. Cui, X. Liu, X. Tong and N. Yang, *Adv. Energy Mater.*, 2022, **12**, 2201548.

